

Article

CO₂ Capture in A Bubble-Column Scrubber Using MEA/CaCl₂/H₂O Solution—Absorption and Precipitation

Pao Chi Chen * and Shiun Huang Zhuo

Department of Chemical and Materials Engineering, Lunghwa University of Science and Technology, Taoyuan 33306, Taiwan; doraemon31906@gmail.com

* Correspondence: chenpc@mail2000.com.tw

Received: 15 June 2020; Accepted: 7 August 2020; Published: 11 August 2020



Abstract: This study used the solvent monoethylamine (MEA)/CaCl₂/H₂O to investigate CO₂ absorption and CaCO₃ crystallization in a bubble column scrubber. The variables explored were pH, gas flow rate, gas concentration, the liquid flow rate of the solution to absorb CO₂, and CaCO₃ crystallization. Under a continuous mode, the solution of CaCl₂ was fed continuously, and the pH dropped after CO₂ absorption. To maintain the set pH value, there was an automatic input of the MEA solvent into the bubble column. In addition to maintaining the pH, the solution could also absorb CO₂ and produce CaCO₃ crystals, which served two purposes. The results showed that there were mainly vaterite crystals. At different pH values, the lower the pH, the higher the precipitation rate of vaterite (F_p), and vice versa. However, under different gas flow rates, the F_p decreased as the pH value increased. Additionally, the process variables also affected the absorption rate (R_A) and the overall mass-transfer coefficient (K_{GA}) generally increased with increasing pH, gas concentration, and gas flow rate. However, it slowed down under operating conditions at high pH and high gas flow rate. Finally, correlation equations for R_A , K_{GA} , and F_p were also obtained and discussed in the study.

Keywords: absorption; precipitation; bubble column scrubber

1. Introduction

The weather irregularity resulting from the greenhouse effect is a matter of great concern around the world. A major portion of greenhouse gases is CO₂, which is mainly caused by the excessive use of fossil fuels and unchecked deforestation [1,2]. Many countries are working towards alternative energy development [3], energy-saving, and process improvement. Chemical treatment, physical treatment, and microbiological treatment are the primary technologies for disposing of the CO₂ emitted from factories, and the most commonly used method used is chemical treatment [4,5]. More than 1000 factories have developed the alkanolamine processes over the past few decades, among which the monoethylamine (MEA) process has the advantages in terms of price, characteristics, and recovery, although, it still consumes energy during recovery and brings cost burdens due to the treatment of concentrated CO₂ [5]. To develop an energy-saving process, new solvents [6–10], and new processes [11,12] have been proposed and explored to find a process with a lower regeneration energy requirement. Some of them studied the absorption kinetics of the mixed solvents [9,13,14]. Alternatively, the hot potassium carbonate process is also applied in many cases, however, solvent regeneration and reuse during recovery not only increases the cost but also causes secondary pollution [1,15]. The issue with the NaOH process is that the solvent cannot be recovered. For the processes focusing on resource recycling, the hot potassium carbonate and the NaOH processes are less effective. Hence, this research team has developed the Ca(OH)₂ process for CO₂ absorption, which can recover CO₂ and produce

CaCO₃ without solvent recovery. However, due to the inability of continuous operation, the process development was limited. Eventually, the process was changed, and BaCl₂/NaOH/H₂O was used for CO₂ absorption, which could produce BaCO₃ and be operated continuously [16,17]. However, limitations still exist in solvent reuse. Previous studies showed that the CO₂ absorption rate is greatly affected by pH because while an increase in pH improves the CO₂ removal efficiency, it consumes more NaOH, which raises the cost. In addition, an increase in the liquid flow rate improves the yield of BaCO₃, and an increase in the gas flow rate improves the CO₂ removal efficiency.

To develop CO₂ and for resource recycling, this team also tried to recover CO₂ and produce CaCO₃ by MEA/CaCl₂/H₂O, and tested solvent reuse. The results showed that the recovered solvent can also absorb CO₂, which motivated us to develop this process. Hence, because of the advantage of the bubble column, with MEA/CaCl₂/H₂O as the solvent, CO₂ recovery and resource recycling were carried out by continuously operating a bubble column [18–21].

The main equations for the reaction with MEA/CaCl₂/H₂O as the solvent are as follows [8,22]:



Equations (1), (4) and (5) present the change in the hydrolysis of the carbonate ion, and Equations (6), (7) present the reaction of using MEA solution for CO₂ absorption. RNCOO[−](aq) is hydrolyzed into HCO₃[−] and RNH₂ after production and then reacts with Ca²⁺ to precipitate CaCO₃ because HCO₃[−] can be further dissociated to CO₃^{2−}. MEA exhibits excellent absorption efficiency, therefore, it has been adopted in several studies.

In the previous studies, to understand the relationship between absorption and crystallization in this system, the quasi-steady operation and shell balance were adopted to obtain the equation of absorption rate, and a two-film model was used to describe the mass transfer of CO₂ in the absorption solvent to determine the overall mass transfer coefficient [16,23]. Hence, the results of this study were compared with those of the previous studies in terms of the above-mentioned theory to understand the commercial value of this process. Further, the yield of the recovered solid was determined by the liquid flow rate and suspension concentration, and the relationship between absorption rate and precipitation rate was used to obtain the design parameters of the absorber.

As a result, with MEA/CaCl₂/H₂O as the absorbent, MEA as the controller of the pH of the system, CaCl₂ as the precipitant, and pH value, CO₂ concentration and CO₂ flow rate as the variables, this study aimed to investigate the effects of variables on the absorption rate, mass transfer coefficient, and precipitation rate by CO₂ absorption experiment in the bubble column, so as to provide references for the design of such absorbers.

2. Absorption Rate and Mass Transfer Coefficient

The gases A (CO₂) and B (N₂) were mixed and added to the bubble column, and the calcium chloride aqueous solution and MEA solvent were separately imported into the bubble column. At the

beginning of the experiment, the calcium chloride solution was continuously fed at 50 mL/min and the MEA was fed to adjust the decline of pH value due to CO₂ absorption to keep it within the set range. MEA balanced pH value and absorbed the CO₂. The absorbed CO₂ decomposed to CO₃²⁻ in the solution and quickly reacted with Ca²⁺ in the solution to form CaCO₃ precipitation. CO₂ was continuously fed and MEA was fed to maintain absorption, finally, the CO₂ at the outlet was steady, indicating that the system was now stable. The mass balance at a steady state of CO₂ is shown below [16]:

$$F_{A1} - F_{A2} - R_A V_L = 0 \quad (10)$$

where, F_{A1} and F_{A2} , respectively, denote the molar flow rates at the CO₂ inlet and outlet, V_L represents the liquid volume in the bubble column and R_A represents the CO₂ absorption rate, which can be obtained by the following equation:

$$R_A = \frac{F_{A1}}{V_L} \left[1 - \left(\frac{1 - y_1}{y_1} \right) \left(\frac{y_2}{1 - y_2} \right) \right] \quad (11)$$

where, y_1 and y_2 , respectively, denote the CO₂ concentrations at the inlet and outlet. Once the absorption rate is obtained, the overall mass transfer coefficient can be obtained by the following equation:

$$K_G a = \frac{R_A}{[C_g - HC_L]_{av}} \quad (12)$$

where, H is Henry's law constant and a function of temperature and ionic strength. In Equation (12), because of the change in the position of the gas as it passes through the bubble column, $C_g - HC_L$ is substituted by the average value of the inlet and outlet, thus, the calculated overall mass transfer coefficient is the average value [23]. However, H -value was found to be 0.39–0.78 [24] and CO₂ in the liquid phase was less than 10⁻⁶ M. Due to this, the value HC_L was less than 10⁻⁶ [25], which was much smaller than C_g . Therefore, the HC_L value can be negligible compared to C_g .

3. Experiment

The major equipment used in this experiment is shown in Figure 1, including the bubble column, digital pressure indicator, heater, CO₂ meter, condenser, pH controller, gas mixer, N₂ cylinder, CO₂ cylinder, and gas flow-meter. The reagents used in this experiment are calcium chloride, MEA, CO₂, and N₂ gas.

Before the experiment, the pH electrode was calibrated with a standard buffer solution of pH 4.0 and 7.0 to accurately observe the change in pH. CO₂ and N₂ cylinders were opened to adjust the flow of CO₂ and N₂ and the gas temperature at the inlet until the CO₂ concentration and temperature of the gas mixer reached the set values. During the experiment, the prepared solution was added into the bubble column, and the gas in the gas mixer was introduced into the solution in the bubble column. To begin the operation, the condenser was opened and the calcium chloride solution was continuously fed at 50 mL/min and the MEA was fed to adjust the decline of pH after absorption to keep it within the set range. On the other hand, CO₂ could be absorbed. The time, pH value, the test value of the CO₂ meter, and MEA feeding volume were recorded during the experiment, and about 5 mL of suspension was extracted in a fixed time. After the suspension was filtered, two additional 5 mL samples of the suspension were taken at 40 and 50 min to measure the calcium ion concentration and total carbonate ion concentration by atomic absorption (AA) (GBC Scientific Equipment, GBC 932 Plus, Melbourne, Australia) At the end of the experiment, an additional 2 mL of suspension was taken and placed in a container used for particle size measurement to measure the size of CaCO₃ particles by using a laser particle size analyzer (Galai CIS-50, Or Akiva, Isreal).

After the experiment, the suspension reacted in the bubble column was filtered, and the obtained solid was dried using a hot air drier. Finally, the obtained powder was weighed, and part of it was observed by a SEM (Jeol, JSM-6500F, Tokyo, Japan) for its morphology, while the other part was

observed by XRD(Rigaku, D/MAX-2200/PC, Tokyo, Japan) components and construction. Table 1 shows the operating conditions of the experiment, with the CO₂ concentration between 10 and 30%, the gas flow rate between 2 and 8 L/min, and the pH value between 9 and 11. Table 1 was the operating conditions conducted in this study.

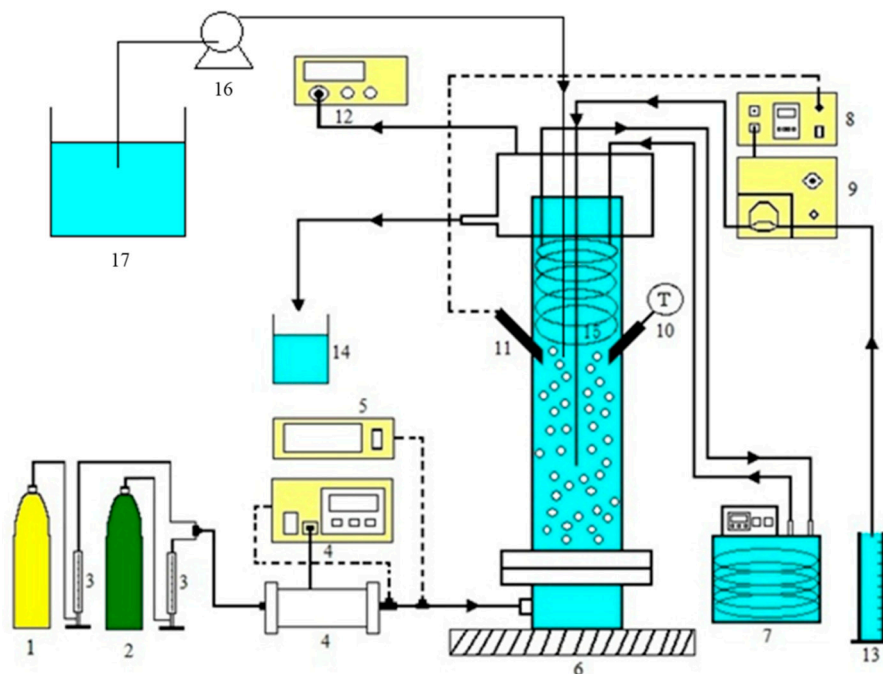


Figure 1. The capture of CO₂ using a bubble-column scrubber. 1. CO₂ gas tank; 2. N₂ gas tank; 3. gas-flow meter; 4. gas-flow meter; 5. digital pressure gauge; 6. bubble-column scrubber; 7. cooling machine; 8. tubing pump; 9. controller; 10. thermometer; 11. pH-electrode; 12. CO₂ meter; 13. MEA solvent reservoir; 14. reservoir; 15. cooling coil; 16. tubing pump; 17. CaCl₂ solution reservoir.

Table 1. Operating conditions used in this work.

Concentration of CO ₂ Gas (%)	10–30
Concentration of CaCl ₂ (M)	0.2
Concentration of MEA (M)	4
Gas-flow rate (L/min)	2–8
Flow rate of CaCl ₂ (mL/min)	50
Gas inlet temperature (°C)	30
Temperature in the column (°C)	35
pH	9–11

4. Results and Discussions

4.1. Experimental Data

Figure 2 shows the CO₂ concentrations at the outlet measured at $Q_g = 4$ L/min and different pH values, indicating that, at pH 9 and 10, the CO₂ concentration at the outlet declined in the initial stage of the experiment, then began to rise nearly 5 min later, and reached a steady state at nearly 40 min and 34 min, respectively. At pH 11, the CO₂ concentration at the outlet first rose and then began to decline nearly 2 min later until it reached a steady state at about 20 min. After the steady state was reached, the absorption rate, mass transfer coefficient, mean residence time, and precipitation rate could be obtained by Equations (10) and (11), by which the precipitation rate was calculated by multiplying the slurry density by the liquid flow-rate and dividing the result by the liquid volume; the mean particle size was measured by the particle size analyzer. As shown in Table 2, the obtained absorption

rate was between 6.26×10^{-6} and 3.80×10^{-4} mol/s·L, the mass transfer coefficient was in the range between 1.83×10^{-3} and 5.33×10^{-2} 1/s, the precipitation rate is was in the range of 0.53×10^{-5} to 26.08×10^{-5} mol/s·L, and the particle size was in the range of 0.72 to 1.83 μm . Further, the absorption efficiency was found to be in the range of 32.8–100%.

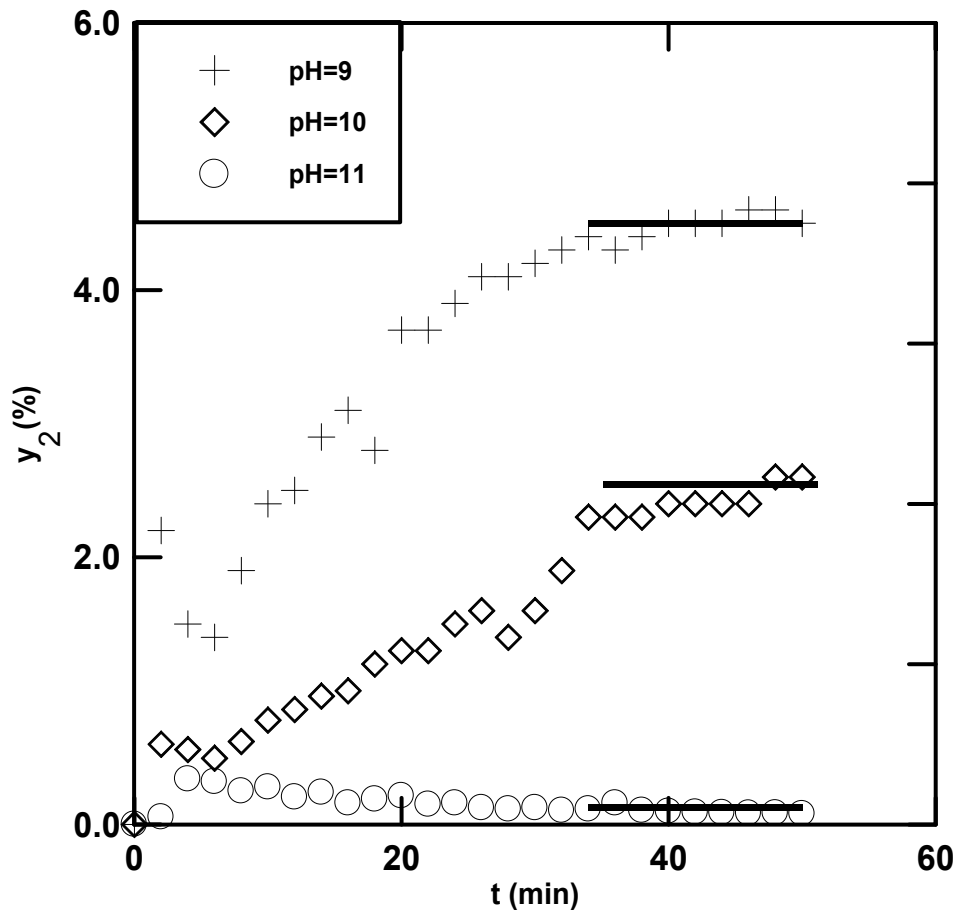


Figure 2. Variation in CO_2 concentration at the outlet with time at different pH values. ($\text{CO}_2 = 10\%$, $Q_g = 4$ L/min).

Table 2. The data obtained in the experiment.

No.	pH	y_1 (%)	u (cm/s)	$R_A \times 10^5$ (mol/s·L)	$K_G a \times 10^2$ 1/s	τ min	$F_p \times 10^5$ (mol/s·L)	E (%)	d_p μm	Q_{add} (mL/min)
1	9	10	1.7	0.63	0.183	17.00	3.42	32.8	1.60	2.0
2	10	10	1.7	1.28	0.487	16.71	1.35	71.5	1.37	2.9
3	11	10	1.7	1.82	0.889	16.01	0.53	100	1.45	2.6
4	9	10	3.4	2.40	1.38	14.98	14.71	55	1.33	9.0
5	10	10	3.4	3.07	1.54	13.92	6.11	75	1.41	13.5
6	11	10	3.4	3.88	2.66	13.56	1.34	99.2	1.83	15.2
7	9	10	5.1	5.02	1.59	9.57	11.59	68	1.14	12.4
8	10	10	5.1	7.36	4.26	9.51	2.85	100	0.64	25.3
9	11	10	5.1	7.40	4.10	4.57	1.06	100	1.78	176.6
10	9	10	6.8	9.78	3.74	11.88	13.76	84.1	1.01	20.2
11	10	10	6.8	14.4	4.31	7.70	10.68	100	0.94	44.3
12	11	10	6.8	11.5	5.20	4.95	3.08	100	1.28	228.4
13	9	20	3.4	12.3	1.53	14.17	26.08	68.7	1.63	42.4
14	10	20	3.4	16.3	2.70	11.74	9.77	97.5	1.44	43.0
15	11	20	3.4	16.4	3.03	3.90	5.43	100	0.72	143.6
16	9	30	3.4	30.8	2.99	12.60	22.50	73.4	1.65	24.4
17	10	30	3.4	38.0	5.33	9.37	10.30	98.3	1.31	64.8
18	11	30	3.4	36.9	4.76	3.18	1.68	100	0.75	128.6

4.2. Identification of Solid Components

The XRD analysis (Figure 3) shows the comparison with the standard CaCO_3 peak, and the results shows that the major peak intensities, (110), (112), (114), (300), (118), and position of the sample obtained from the experiment were consistent with those of the vaterites as reported earlier [26–28], indicating that the obtained CaCO_3 was mainly vaterite.

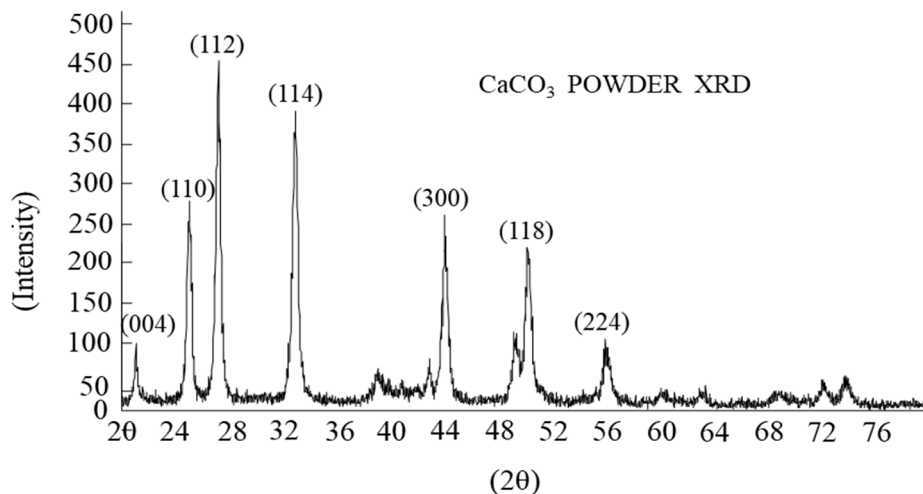


Figure 3. XRD spectra for No. 2 showing the intensity of vaterite.

4.3. Effects of Variables on Vaterite Morphology and Size

Figure 4 shows different morphologies of vaterites with different flow rates observed by SEM when the pH was 9 and y_1 was 10%. According to the images observed by SEM, the single particles were mainly disc vaterites. With the increase in Q_g , the morphology changed a little, but the particle size decreased. The picture in Figure 4a showed the uniform particles were observed; on the other hand, in Figure 4b–d, they showed some tiny particles were formed giving average size smaller. However, the effects of Q_g on particles need to be investigated further. Figures 4b and 5 show the effects of different CO_2 concentrations on the vaterite morphology; the morphology obtained at different CO_2 concentrations was nearly discoid and spherical. Its morphology was nearly spherical when y_1 was 10% ($d_p = 1.33 \mu\text{m}$), 20% ($d_p = 1.63 \mu\text{m}$), and 30% ($d_p = 1.65 \mu\text{m}$), and the mean particle size increased with the increase in y_1 .

Figures 4b and 6 show the different morphologies at different pH values when y_1 was 10% and the flow rate was 4.0 L/min. At pH 9, as shown in Figure 4b, the calcium carbonate morphology was roughly spherical; at pH 10, spherical crystals began to form; at pH 11, the morphology was mainly spherical and significantly exhibited the shape of vaterite, and the particle size increased with the increase in pH value. However, when y_1 was 20% and 30%, the particle size decreased with the increase in pH (Please see Table 2). The possible reason may be that the increase in MEA feed and CO_2 absorption at a high pH improved the rates of supersaturation and nucleation, so that the precipitation increased accordingly, which affected the particle size and morphology.

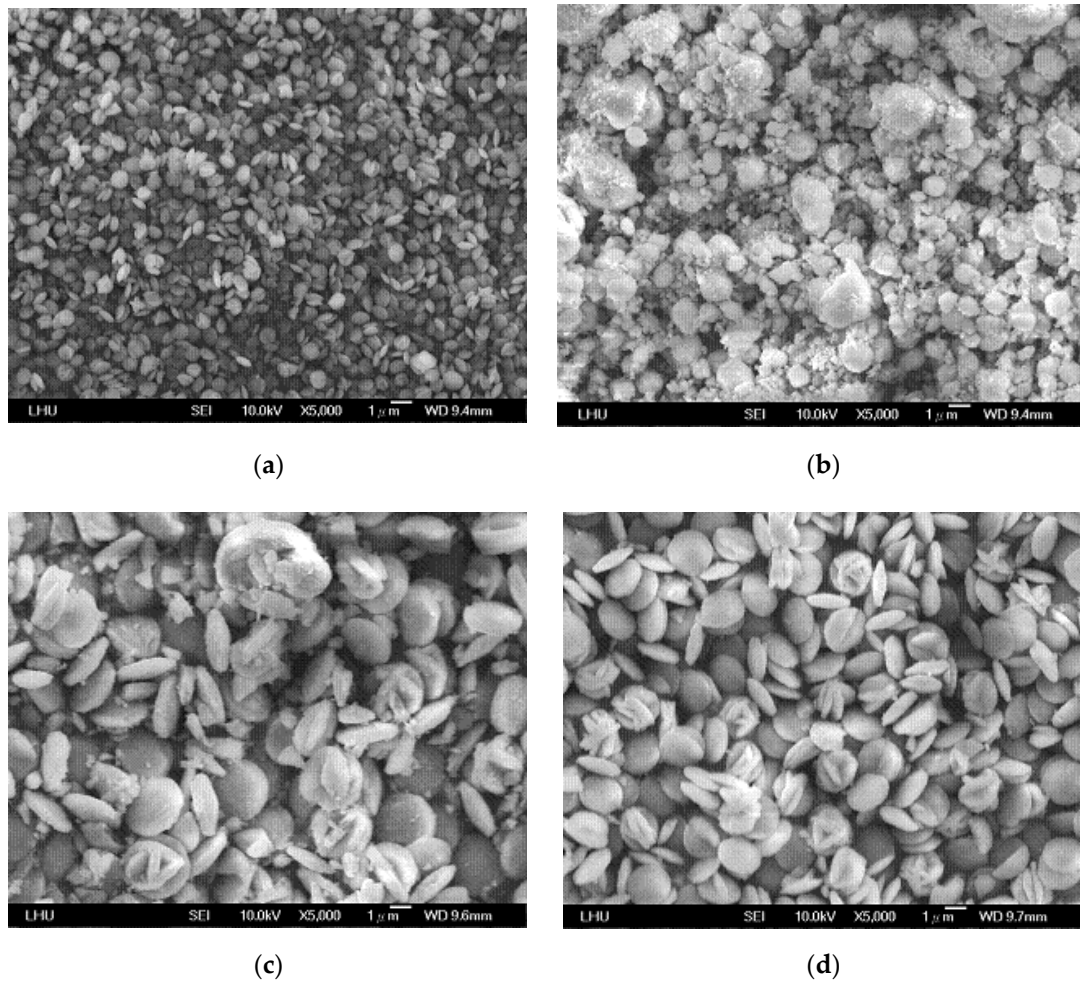


Figure 4. Effects of Q_g on the morphology and crystal size of vaterite. (a) $Q_g = 2$ L/min ($d_p = 1.60$ μm) (No. 1); (b) $Q_g = 4$ L/min ($d_p = 1.33$ μm) (No.4); (c) $Q_g = 6$ L/min ($d_p = 1.14$ μm) (No. 7); (d) $Q_g = 8$ L/min ($d_p = 1.01$ μm) (No. 10).

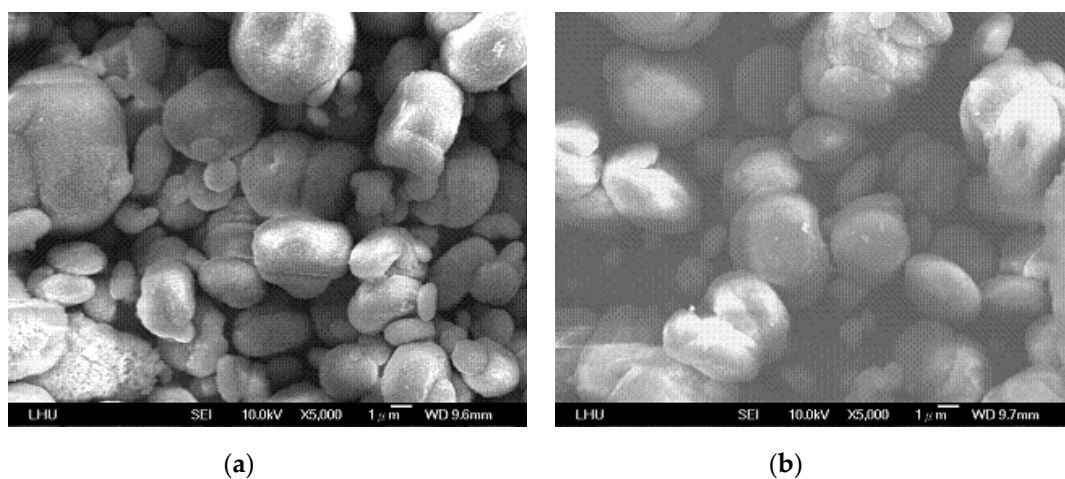


Figure 5. Effects of γ_1 on the morphology and crystal size of vaterite (pH = 9, $Q_g = 4$ L/min). (a) 20% ($d_p = 1.63$ μm) (No. 13); (b) 30% ($d_p = 1.65$ μm) (No. 16).

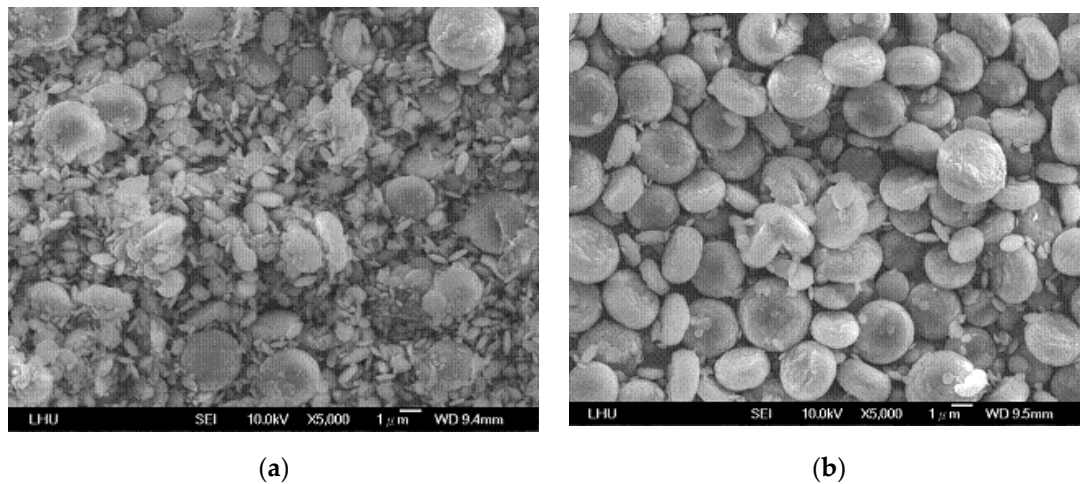


Figure 6. Effects of pH on the morphology and crystal size of vaterite ($y_1 = 10\%$, $Q_g = 4\text{L/min}$). (a) pH = 10 ($d_p = 1.41\ \mu\text{m}$) (No.5); (b) pH = 11 ($d_p = 1.83\ \mu\text{m}$) (No. 6).

4.4. Effects of Variables on the Absorption Rate of CO_2

To investigate the effects of variables on the absorption rate, the pH value at the absorption rate (R_A) was drawn, as shown in Figure 7. In Figure 7a, with the volume flow rate as the parameter, R_A was found to increase roughly with the increase in pH; R_A increased linearly with pH at low flow rates and remained steady with the increase in pH at high flow rates, indicating that the increase in pH had limited effects on the absorption rate. In addition, Figure 7a also shows that, at high flow rates, the absorption rate was high and increased significantly, indicating that increasing the flow rate is an effective method to increase the absorption rate. Finally, as per Figure 7b, the feed concentration significantly increased the absorption rate, but the effects of pH were limited at high values of y_1 .

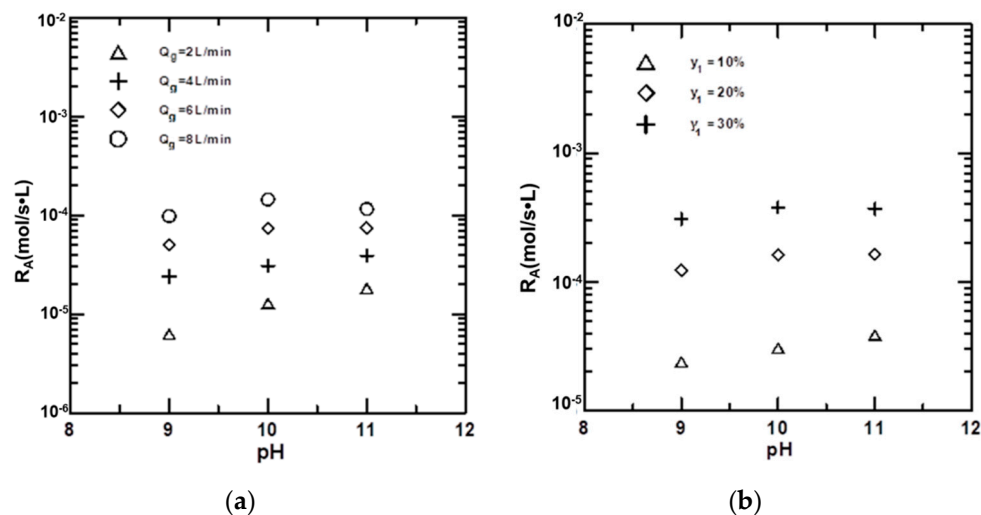


Figure 7. Effects of process variables on the absorption of CO_2 . (a) Effects of pH at different gas-flow rates; (b) Effects of pH at different gas concentrations.

The effects of parameters on R_A were explored using linear regression and the result was as follows:

$$R_A = 6.9095 \times 10^{-5} \exp(0.21pH) y_1^{2.12} u^{1.67} \quad (13)$$

The regression error was 1.63%. The regression confidence is shown in Figure 8. The regression result showed that R_A was proportional to u and y_1 to the powers of 1.67 and 2.12, respectively. It also shows that R_A increased with an increase in pH. In addition, the R_A values presented here were in

the range of 0.063×10^{-4} – 3.8×10^{-4} mol/s·L, which was much smaller than that of MEA-CO₂-H₂O absorption system (3.68×10^{-4} – 56.8×10^{-4} mol/s·L) as reported in the previous study [21]. The difference was due to the formation of vaterites, a larger number of tiny particles, which enhanced the coalescence of the bubbles. Due to this, the mass-transfer rate of CO₂ gas was blocked, which reduced the absorption rate.

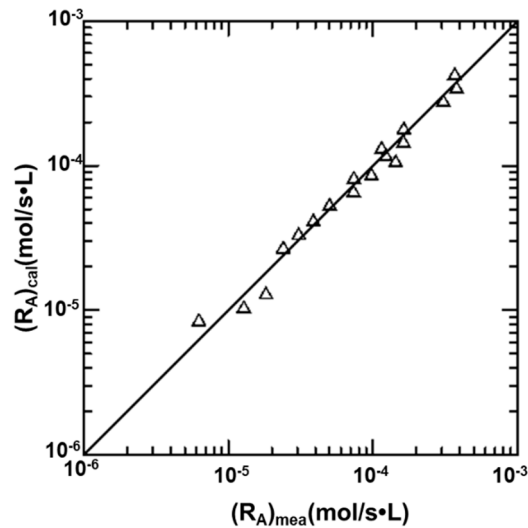


Figure 8. Regression confidence for R_A .

4.5. Effects of Variables on K_{GA}

As shown in Figure 9a, the K_{GA} value increased linearly with the increase in pH, and a higher gas flow rate led to a higher K_{GA} value. At a high pH value (pH = 11), the absorption tended to be complete, as shown in Figure 2, indicating the reduced effects on K_{GA} . Figure 9b shows that K_{GA} increased with the increase in pH and y_1 , and this value was large at a high pH. The figure also shows that, at pH = 10 and 11, the K_{GA} values were leveled off, indicating the diminishing effects of pH.

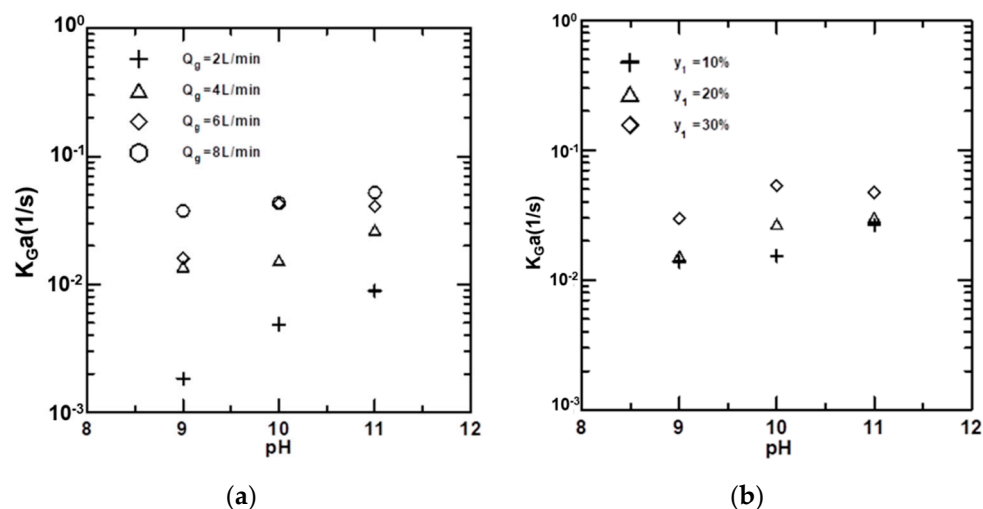


Figure 9. Effects of variables on the K_{GA} at different conditions. (a) Effects of pH at different gas-flow rates; (b) Effects of pH at different gas concentrations.

The relationship between K_{GA} and pH value, and between u and y_1 was explored, and K_{GA} was used to carry out a regression analysis of u , y_1 and pH, and the result was as follows:

$$K_{GA} = 2.8469 \times 10^{-4} u^{1.68} y_1^{0.87} \exp(0.39pH) \quad (14)$$

The regression error was 6.42%. The difference between the calculated value and the measured value is presented in Figure 10. The regression result showed that K_{GA} was proportional to u to the power of 1.68 and the obtained value was closer than that reported earlier, which was between 0.58 and 1.67 [7,9–12], and the empirical formula also shows that K_{GA} increased with the increase in y_1 and pH value. The overall mass transfer coefficients at different pH values, y_1 , and u could be estimated from Equation (14), and after the values were determined, the volume of the absorption tower could be estimated. In addition, the difference in the mass transfer coefficient in the bubble columns can be compared with each other. For example, please see Table 3. The values obtained in this study ranged from 0.01 to 0.15 1/s, congruent with those reported in the literature [29–33]. However, these values were much smaller than those reported in previous work [21], and those by Al-Naimi et al. [29]. In our study, as shown in Table 2, K_{GA} decreased with an increase in F_p , such as that in No.1-No.3. In addition, in other earlier studies [23] we found that Nos. 7(0.0136 1/s), 8(0.0199 1/s), 10(0.0506 1/s), 11(0.0299 1/s), 12(0.0241 1/s) were lower in mass-transfer coefficient due to the formation of ABC crystals. This decrease in mass transfer coefficient with increasing solid concentration is attributed to a decrease in small bubble and an increase in large bubble sizes due to the bubble coalescence tendencies, and they exhibited limited the mass transfer coefficient [29]. A similar trend was found in an earlier study [31].

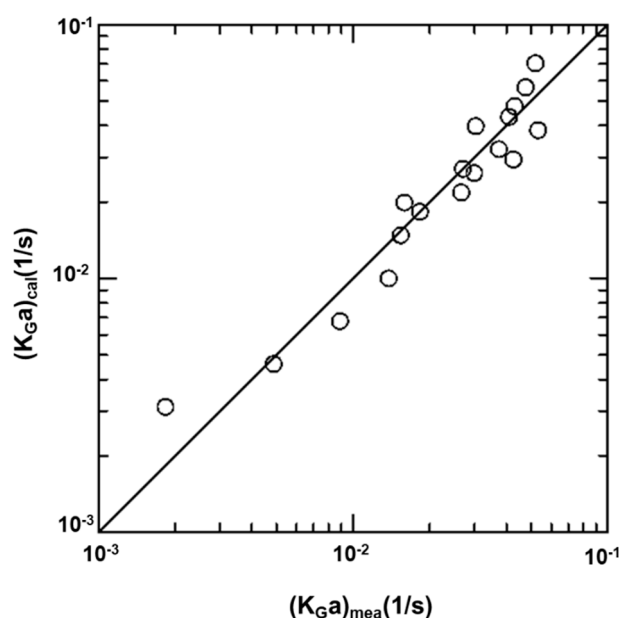


Figure 10. A plot of calculated K_{GA} versus measured K_{GA} .

Table 3. Comparison of mass-transfer coefficients in the bubble columns.

K_{GA} (1/s)	$R_A \times 10^4$ (mol/s·L)	Remarks and References
0.01–0.14	-	O ₂ -Liquid(water/glycerin/alcohol)-Solid(PVC) [29]
0.045–0.085	-	O ₂ (N ₂ +O ₂)-H ₂ O [30]
0.02–0.14	-	Air-Paraffin oil-Porous catalyst [31]
0.01–0.15	-	O ₂ -H ₂ O [32]
0.0377–0.8881	3.68–56.8	CO ₂ -MEA-H ₂ O [21]
0.021–0.109	1.36–6.61	CO ₂ -NaOH-H ₂ O [33]
0.0143–0.3302	3.21–9.03	CO ₂ -NH ₃ -H ₂ O [23]
0.0183–0.0520	0.063–3.80	CO ₂ -MEA-CaCl ₂ -H ₂ O [This work]

4.6. Precipitation Rates of Vaterites

Figure 11 shows the relationship between the rate of CaCO₃ precipitation and pH at different y_1 . The results indicate that the precipitation rate of CaCO₃ increased with the decrease in pH, otherwise,

the precipitation rate decreased. This figure also shows that F_p tended to increase with an increase in y_1 . Figure 12 shows the effects of pH on F_p at different Q_g values and obviously indicates that F_p values decreased with the increase in pH, regardless of Q_g . Moreover, generally, a higher Q_g led to a larger F_p . However, when $Q_g = 8$ L/min, except at pH = 9, F_p was smaller than that at $Q_g = 6$ L/min, which may be caused by the restriction of the system operation.

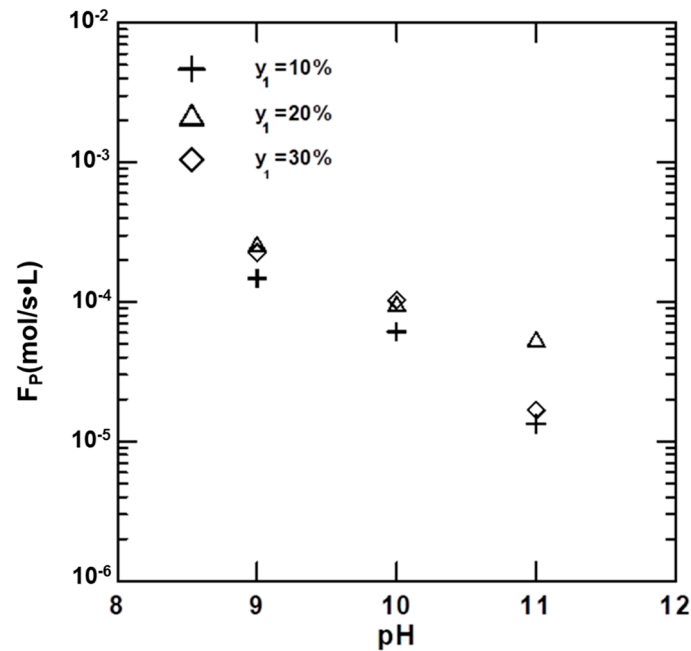


Figure 11. Variation in F_p with pH at different y_1 values.

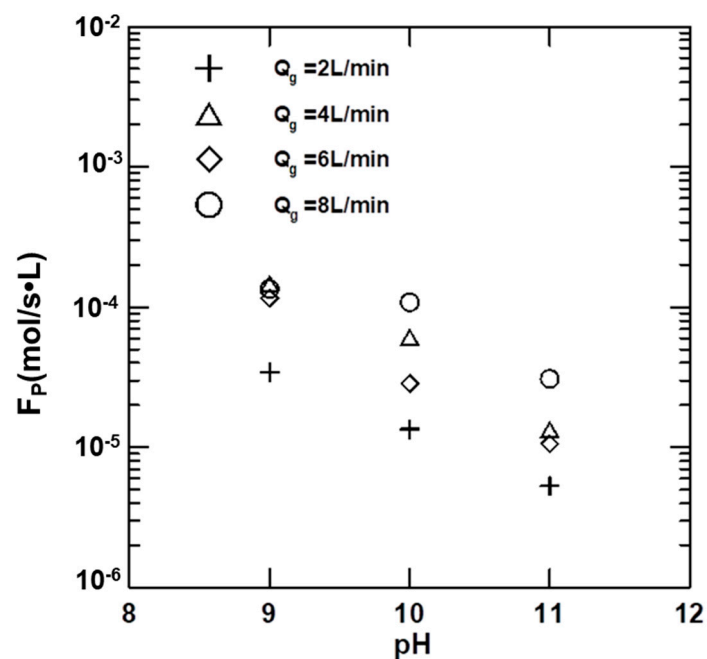


Figure 12. Variation in F_p with pH at different Q_g values.

The results of the above discussion and the data in Table 2 indicate a competition effect between R_A and F_p , which was affected by u , y_1 , and pH . Hence, F_p was used to carry out the regression of parameters for comparison, and the result was as shown below:

$$F_p = 2.5081 \exp(-1.02pH)y_1^{0.98}u^{1.06} \quad (15)$$

The error was 4.28% and the reliability was as shown in Figure 13. According to this equation, the F_p value decreased with the increase in pH and increased with an increase in u and y_1 . Here, we defined the ratio of R_A and F_p as ψ . Using Equations (13) and (15), the relation became $\psi = 2.7548 \times 10^{-5} \exp(1.23pH)y_1^{1.14}u^{0.61}$. A high ψ value indicates that the mass transfer was dominated by absorption, while a low ψ value indicates that the mass transfer was dominated by crystallization.

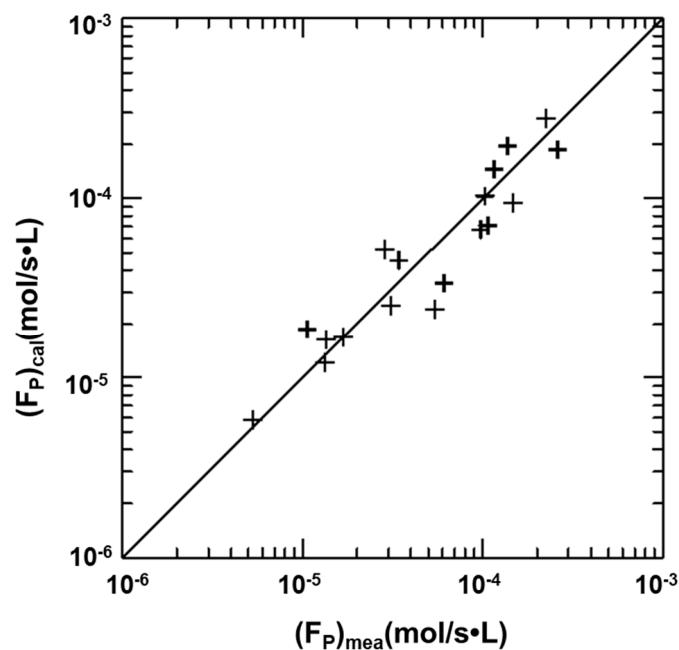


Figure 13. A plot of calculated versus measured ψ showing the confidence of regression.

5. Conclusions

In a continuous bubble column, the vaterite was precipitated mainly in disk-like and spherical morphology if MEA/CaCl₂/H₂O solution was used for CO₂ absorption. At $pH = 11$, regardless of the other conditions, the absorption rate was close to 100%, so the increase in pH made no contribution to the improvement in absorption efficiency. The shell balance and two-film model were able to determine the absorption rate and overall mass transfer coefficient. An improvement in the gas flow rate and gas concentration increased the solid precipitation rate and overall mass transfer coefficient, but the solid precipitation rate decreased with the increase in pH values. Therefore, the precipitation rate was competitive with the absorption rate, which could be estimated by $\psi (= R_A/F_p)$. A high ψ value indicates that the mass transfer was dominated by absorption, while a low ψ value indicates that the mass transfer was dominated by crystallization. The results show that the MEA/CaCl₂/H₂O solution can be used to absorb CO₂, the greenhouse gas, and recover CaCO₃, and is a technology worthy of further development.

Author Contributions: P.C.C. conceived and designed the experiments and wrote the paper, while S.H.Z. performed the experiments and analyzed the data. All authors have read and agreed to the published version of the manuscript.

Funding: This research received no external funding.

Acknowledgments: The authors acknowledge the financial support of the MOST in Taiwan ROC (MOST-109-2221-E-262-004).

Conflicts of Interest: The authors declare no conflict of interest.

References

1. Streedhar, I.; Nahar, T.; Venugopal, A.; Srinivas, B. Carbon capture by absorption—path covered and ahead. *Renew. Sustain. Energy Rev.* **2017**, *76*, 1080–1107. [[CrossRef](#)]
2. Ali Khan, A.; Hader, G.N.; Saha, A.K. Carbon dioxide capture characteristics from flue gas using aqueous 2-amino-2-methyl-1-propanal (AMP) and monoethanolamine (MEA) solutions in packed bed absorption and regeneration columns. *Int. J. Greenh. Gas Control.* **2015**, *32*, 15–23. [[CrossRef](#)]
3. Tian, Y.; Zhao, C.Y. A review of solar collectors and thermal energy storage in solar thermal Applications. *Appl. Energy* **2013**, *104*, 538–553. [[CrossRef](#)]
4. Leung, D.Y.C.; Caramanna, C.; Maroto-Valer, M.M. An overview of current status of carbon dioxide capture and storage technologies. *Renew. Sustain. Energy Rev.* **2014**, *39*, 426–443. [[CrossRef](#)]
5. Yu, C.H.; Huang, C.H.; Tan, C.S. A Review of CO₂ Capture by Absorption and Adsorption. *Aerosol Air Qual. Res.* **2012**, *12*, 745–769.
6. Mangalapally, H.P.; Notz, R.; Hoch, S.; Asprien, N.; Mangalapally, H.P.; Notz, R.; Hoch, S.; Asprien, N.; Sieder, G.; Garcia, H.; et al. Pilot plant experimental studies of post combustion CO₂ capture by reactive absorption with MEA and new solvent. *Energy Procedia.* **2009**, *1*, 963–970. [[CrossRef](#)]
7. Vaidya, P.D.; Kenig, E.Y. Absorption of CO₂ into aqueous blends of alkanolamines prepared from renewable resources. *Chem. Eng. Sci.* **2007**, *62*, 7344–7350. [[CrossRef](#)]
8. Kwak, N.S.; Lee, J.H.; Lee, I.Y.; Jang, K.R.; Shim, J.G. A study of new absorbent for post-combustion CO₂ capture test bed. *J. Taiwan Inst. Chem. Eng.* **2014**, *45*, 2549–2556. [[CrossRef](#)]
9. Hwang, K.S.; Park, S.W.; Park, D.W.; Oh, K.J.; Kim, S.S. Absorption of carbon dioxide into diisopropanolamine solutions of polar organic solvents. *J. Taiwan Inst. Chem. Eng.* **2010**, *41*, 16–21. [[CrossRef](#)]
10. Lee, K.H.; Lee, B.; Lee, J.H.; You, J.K.; Park, K.T.; Baek, I.H.; Hur, N.H. Aqueous hydrazine as a promising candidate for capturing carbon dioxide. *Inter. J. Greenh. Gas Control* **2014**, *29*, 256–262. [[CrossRef](#)]
11. Zhao, B.; Su, Y.; Peng, Y.C. Effect of reactor geometry on aqueous ammonia-based carbon dioxide capture in bubble column reactors. *Inter. J. Greenh. Gas Control* **2013**, *17*, 481–487. [[CrossRef](#)]
12. Andersson, V.; Franck, P.A.; Berntsson, T. Industrial excess heat driven post-combustion CCS: The effect of stripper temperature level. *Inter. J. Greenh. Gas Control* **2014**, *21*, 1–10. [[CrossRef](#)]
13. Xiao, J.; Li, C.C.; Li, M.H. Kinetics of absorption of carbon dioxide into aqueous solutions of 2-amino-2-methyl-1-propanol + monoethanolamine. *Chem. Eng. Sci.* **2000**, *55*, 161–175. [[CrossRef](#)]
14. Lin, C.Y.; Soriano, A.N.; Li, M.H. Kinetics study of carbon dioxide absorption into aqueous solution containing N-methyldiethanolamine + Diethanolamine. *J. Taiwan Inst. Chem. Eng.* **2009**, *40*, 403–412. [[CrossRef](#)]
15. Borhani, T.N.G.; Azarpour, A.; Akbari, V.; Wan Alwi, S.R.; Manan, Z.A. CO₂ capture with potassium carbonate solutions: A state-of-the-art review. *Inter. J. Greenh. Gas Control* **2015**, *41*, 142–162. [[CrossRef](#)]
16. Chen, P.C.; Shi, W.; Du, R.; Chen, V. Scrubbing of CO₂ greenhouse gases, accompanied by precipitation in a continuous bubble-column scrubber. *Ind. Eng. Chem. Res.* **2008**, *47*, 6336–6343. [[CrossRef](#)]
17. Chen, P.C.; Shi, W.; Du, R.; Chen, V. Crystallization kinetics of barium carbonate crystals in a lab-scale bubble-column scrubber. *J. Taiwan Inst. Chem. Eng.* **2014**, *45*, 2418–2426. [[CrossRef](#)]
18. Chen, P.C. *Absorption of Carbon Dioxide in a Bubble Column Scrubber*. *Greenhouse Gases*; Liu, G., Ed.; InTech: Rijeka, Croatia, 2012; Chapter 5; pp. 95–116.
19. Petrov, P.; Ewert, G.; Rohm, H.J. Chemisorptive removal of carbon dioxide from process streams using a reactive bubble column with simultaneous production of usable materials. *Chem. Eng. Technol.* **2006**, *29*, 1084–1089. [[CrossRef](#)]
20. Sánchez, O.; Michaud, S.; Escudié, R.; Delgenès, J.-P.; Bernet, N. Liquid mixing and gas–liquid mass transfer in a three-phase inverse turbulent bed reactor. *Chem. Eng. J.* **2005**, *114*, 1–7. [[CrossRef](#)]
21. Chen, P.C.; Luo, Y.X.; Cai, P.W. CO₂ Capture using monoethanolamine in a bubble-column scrubber. *Chem. Eng. Technol.* **2015**, *38*, 274–282. [[CrossRef](#)]
22. Vaidya, P.D.; Kenig, E.Y. CO₂-alkanolamine reaction kinetics: A review of recent studies. *Chem. Eng. Technol.* **2007**, *11*, 1467–1474. [[CrossRef](#)]

23. Chen, P.C.; Yu, S.C. CO₂ capture and crystallization of ammonia biocarbonate in a lab-scale scrubber. *Crystals* **2018**, *8*, 39. [[CrossRef](#)]
24. Li, L.; Maeder, M.; Burns, R.; Puxty, G.; Clifford, S.; Yu, H. The Henry coefficient of CO₂ in the MEA-CO₂-H₂O system. *Energy Procedia* **2017**, *114*, 1841–1847. [[CrossRef](#)]
25. Tong, D.; Martin Trusler, J.P. Solubility of carbon dioxide in aqueous solution on monoethanolamine or 2-amino-2-methyl-1-propanal: Experimental measurements and modeling. *Inter. J. Greenh. Gas Control* **2012**, *6*, 37–47. [[CrossRef](#)]
26. Li, Q.; Ding, Y.; Li, F.; Xie, B.; Qiana, Y. Solvothermal growth of vaterite in the presence of ethylene glycol, 1,2-propanediol and glycerin. *J. Crystal Growth* **2002**, *236*, 357–362. [[CrossRef](#)]
27. Trushina, D.B.; Bukreeva, T.V.; Kovalchuk, M.V.; Antipina, M.N. CaCO₃ vaterite microparticles for biomedical and personal care applications. *Mater. Sci. Eng. C* **2014**, *45*, 644–658. [[CrossRef](#)]
28. Brecevic, L.; Kralj, D. On calcium carbonates: From fundamental research to application. *Croatia Chem. Acta* **2007**, *80*, 467–484.
29. Al-Naimi, S.A.; Salih, S.A.J.; Al-Atabi, H. Simulation study of mass transfer coefficient in slurry bubble column reactor using neural network. *Al-Khwarizmi Eng. J.* **2013**, *9*, 60–70.
30. Lau, R.; Lee, P.H.V.; Chen, T. Mass transfer studies in shallow bubble column reactors. *Chem. Eng. Process. Process Intensif.* **2012**, *62*, 18–25. [[CrossRef](#)]
31. Vandu, C.O.; Koop, K.; Krishna, R. Volumetric mass transfer coefficient in a slurry bubble column operating in the heterogeneous flow regime. *Chem. Eng. Sci.* **2004**, *59*, 5417–5423. [[CrossRef](#)]
32. Dhaouadi, H.; Poncin, S.; Hornut, J.M.; Midoux, N. Gas–liquid mass transfer in bubble column reactor: Analytical solution and experimental confirmation. *Chem. Eng. Process* **2008**, *47*, 548–556. [[CrossRef](#)]
33. Chen, P.C.; Chou, P.H.; Lin, S.Z.; Chen, H.W. Capturing CO₂ by using a microalgae culture recycle solution. *Chem. Eng. Technol.* **2017**, *40*, 2274–2282. [[CrossRef](#)]



© 2020 by the authors. Licensee MDPI, Basel, Switzerland. This article is an open access article distributed under the terms and conditions of the Creative Commons Attribution (CC BY) license (<http://creativecommons.org/licenses/by/4.0/>).